Efficiency enhancement in photoelectrochemical water splitting: Defect passivation and boosted charge transfer kinetics of zinc oxide nanostructures via chalcopyrite/chalcogenide mix sensitization

Cigdem Tuc Altaf,[1] Nazrin Abdullayeva,[1] Ozlem Coskun,[1] Alihan Kumtepe,[1] İpek Deniz Yildirim,[2] Emre Erdem,[2] Maochang Liu,[3] Ali Bozbey,[4] Ertan Agar,[5] Mehmet Sankir,[1,6,*] and Nurdan Demirci Sankir[1,6,†]

[1]*Micro and Nanotechnology Graduate Program, TOBB University of Economics and Technology, Sogutozu Caddesi No 43 Sogutozu, 06560 Ankara, Turkey*

[2]*Faculty of Engineering and Natural Sciences, Sabanci University, Orhanli, Tuzla, 34956 Istanbul, Turkey*

[3]*International Research Center for Renewable Energy, State Key Laboratory of Multiphase Flow in Power Engineering, Xi'an Jiaotong University, Xi'an, Shaanxi 710049, People's Republic of China*

[4]*Department of Electrical and Electronics Engineering, TOBB University of Economics and Technology, Sogutozu Caddesi No 43 Sogutozu, 06560 Ankara, Turkey*

[5]*Department of Mechanical Engineering, Energy Engineering Graduate Program, University of Massachusetts Lowell, Lowell, Massachusetts 01854, USA*

[6]*Department of Materials Science and Nanotechnology Engineering, TOBB University of Economics and Technology, Sogutozu Caddesi No 43 Sogutozu, 06560 Ankara, Turkey*

(Received 23 July 2021; revised 5 November 2021; accepted 23 November 2021; published 8 December 2021)

ZnO thin films in nanorod (NR) and nanoflower (NF) morphologies were used as photoelectrode scaffolds for efficient visible-light-driven photoelectrochemical (PEC) water splitting process, where their decoration with copper indium gallium sulfide (CIGS) and indium sulfide (In_2S_3) layers resulted in significant PEC performance enhancement. ZnO NF/CIGS/In_2S_3 photoelectrodes exhibited a remarkably high PEC efficiency (~6.0% applied bias photon-to-current efficiency, 83% incident photon-to-current efficiency) due to the negligible dark current, while ZnO NR/CIGS/In_2S_3 generated a photocurrent density of 30.0 mA.cm^{-2} at 0.4 V (vs Ag/AgCl), being one of the highest performances reported in the literature for copper-based chalcopyrite photoelectrodes so far. The interfacial photoelectrode-electrolyte charge transport dynamics, investigated via intensity-modulated photocurrent spectroscopy, exhibited a sevenfold increase in charge transfer efficiencies with a significant drop in surface recombination kinetics for ZnO NF after CIGS/In_2S_3 decoration. The obtained results show consistency with numerically modeled electric field distribution profiles and electron paramagnetic resonance results of ZnO NF, rationalizing the enhanced charge transfer rates for decorated samples and confirming the defect passivating nature of CIGS/In_2S_3.

DOI: 10.1103/PhysRevMaterials.5.125403

I. INTRODUCTION

Humankind must instantly hasten the progress of renewable energy to reduce greenhouse gas emissions caused by fossil fuel consumption [1]. In this regard, the utilization of solar radiation as a high-capacity energy source to achieve sustainable energy for replacing fossil fuels has been considered as a feasible method to unravel environmental issues. The photoelectrochemical (PEC) water splitting process, employing semiconducting materials for the direct conversion of solar energy into hydrogen gas, has been considered as an alternative renewable energy conversion technique to decrease the consumption of traditional fuels [2–5]. Optical and electrical properties, as well as the efficiency and stability of the photoelectrode materials, are the key factors to achieve successful PEC water splitting [6–8].

Zinc oxide (ZnO) is one of the most promising and thoroughly investigated photoanode materials owing to its excellent properties, such as nontoxic nature, the direct bandgap of ~3.3 eV, and high photosensitivity [9–11]. Additionally, the cost-effective manufacturing routes of ZnO at low temperatures result in various morphologies such as nanorod (NR), nanowire (NW), nanotube, nanosheet, and nanoflower (NF) structures depending on the growth conditions [9,12,13]. Previously, the effect of morphology of the metal oxide nanostructures on PEC performance has been reported [9,12]. Based on the literature, it can be concluded that nanostructured photoelectrodes resulted in better solar water splitting performance due to the enhancement of light trapping and surface interactions. However, there is still a need to further increase the PEC energy conversion efficiency of metal-oxide-based electrodes. Hence, intensive effort is put into the design of visible-light-active photoelectrodes with high efficiency and stability for utilizing maximum sunlight. Metal doping and sensitizing with another semiconductor having a narrower bandgap are some of the commonly encountered ways to increase the light activity of ZnO-based photoelectrode materials [14].

Copper-based semiconductors in the chalcopyrite crystal phase such as $CuInS_2$, $CuGaS_2$, Cu(In, Ga)S_2, and

*msankir@etu.edu.tr
†nsankir@etu.edu.tr; ndsankir@gmail.com

 ©2021 American Physical Society

Cu(In,Ga)S,Se are considered auspicious light absorber materials in photovoltaic (PV) applications [15–18]. Additionally, for copper indium gallium sulfide (CIGS)-based PV devices, cadmium sulfide (CdS), which is found to be extremely supportive in diminishing the recombination for enhanced efficiencies, is the most commonly encountered buffer layer material [19–21]. Consequently, CIGS-based solar cells with a CdS buffer layer have been reported to reach record efficiencies [22,23]. After these fruitful results obtained in the PV area, chalcopyrite members have started to be implemented in PEC water splitting systems [24–32]. Like PV devices, in PEC applications of chalcopyrite-based photoelectrodes, CdS has also been used to form *p-n* junctions [29,33,34]. However, the highly toxic nature of Cd metal has led researchers to pursue alternative materials for responding to environmental concerns. In this regard, indium sulfide (In_2S_3) has been reported as a possible predominant material over CdS to be used as a buffer layer for chalcopyrite-based photoelectrodes due to its stability and more ecofriendly nature with high carrier mobility ($\sim$17.6 $cm^2\ V^{-1}\ s^{-1}$) and optimum bandgap energy (2.0–2.8 eV) [30,35,36].

Herein, thin film photoanodes containing ZnO NR and NF morphologies exhibit significant differences in optical properties and hence eventuate in ultraviolet (UV)-originated maximum incident photon-current efficiency (IPCE) values of 10 and 40% for NR and NF structures, respectively. Further performance improvement has been achieved by introducing CIGS/In_2S_3 layers to enhance the PEC activity throughout the visible spectrum. The improvement in water splitting performances has been expounded via electron paramagnetic resonance (EPR) and intensity-modulated photocurrent spectroscopy (IMPS) analyses, which examined the surface defect activity and charge transport/recombination dynamics after CIGS/In_2S_3 decoration. Furthermore, the electromagnetic waves module of COMSOL Multiphysics has been implemented as a *fortiori* numerical analysis to simulate the electric field distribution of both pristine and CIGS/In_2S_3-decorated ZnO nanostructures.

II. EXPERIMENTAL SECTION

A. Fabrication of photoelectrodes

Thin film photoelectrodes were prepared via chemical bath deposition (CBD) and ultrasonic spray pyrolysis (USP) methods in a sequence as depicted in Fig. S1 in the Supplemental Material [37]. Briefly, CBD deposition of ZnO nanostructures on the fluorine-doped tin oxide (FTO) coated glass substrates resulted in NF and NR morphologies by altering the anionic species [9]. However, before the CBD process, we deposited the ZnO seeding layer on FTO glass substrates via radiofrequency magnetron sputtering (ZnO target with 99.999% purity, Plasmaterials) at 60 W for 7 min followed by rapid thermal annealing at 300 °C for 30 min (3 °C/s). The growth of ZnO NF morphology on processed substrates was attained using a 100 mL aqueous solution of urea [$CO(NH_2)_2$, 0.1 mol, 6.03 g] and zinc nitrate hexahydrate [$Zn(NO_3)_2 6H_2O$, 0.005 mol, 1.48 g]. The pH of the CBD solution was set to 5.4 by adding nitric acid dropwise. The substrates were kept vertically in CBD solution at 80 °C for 3 h to form ZnO NF thin films. The reaction was ended by rinsing the substrates in distilled water followed by calcination at 300 °C for 30 min. On the other hand, ZnO NR morphology was obtained in a 100 mL aqueous solution of zinc chloride ($ZnCl_2$, 0.003 mol, 0.41 g) and hexamethylenetetramine (HMTA, 0.005 mol, 0.84 g) at 80 °C for 3 h. The reaction was quenched after placing the reactor in an ice bath for 2 min followed by rinsing ZnO thin films in water. The calcination step was not applied for ZnO NR morphologies. CIGS and In_2S_3 layers were deposited on the nanostructured ZnO thin films via the USP method as described in our previous works [16,30,38]. A schematic illustration for the fabrication of the inversely configurated photoelectrodes is given in Fig. S1(a) in the Supplemental Material [37].

B. Material characterization

Environmental scanning electron microscopy (ESEM) analysis was performed via QUANTA 400F Field Emission SEM. X-ray diffraction (XRD) analysis, which allows us to identify the differences in crystallographic phase and crystallinity of ZnO thin films, was performed with PANalytical/Philips X'Pert MRD system. UV/Vis (Perkin Elmer, Lambda 650S) was used to collect transmission (T) and reflectance (R) data using the bare FTO coated glass substrate as a reference. The absorbance spectra of the thin films were obtained from the evaluation of R and T data using the formula $A = 1 - (T + R)$ [39]. X-ray absorption spectroscopy measurements consisting of extended x-ray absorption fine structure (EXAFS) and x-ray absorption near-edge spectroscopy (XANES) of Zn K-edges were made at the XAFS/XRF beamline at Synchrotron-light for Experimental Science and Applications in the Middle East (SESAME) synchrotron light source located in Allan, Jordan. Because of the variation in sample thicknesses, room-temperature EXAFS analysis data at the Zn K-edge were gathered from 9625 to 9800 eV in fluorescence and transmission modes for both ZnO thin films. ATHENA and ARTEMIS software were used for the raw x-ray absorption data processing. PHI VersaProbe was used to conduct x-ray photoelectron spectroscopy (XPS) analysis. The collected data were corrected with respect to the C1s internal reference peak of graphitic carbon (BE = 285 eV) [40]. Additionally, individual O1s spectra of both nanostructures were fitted into corresponding Gaussian peaks via ORIGINPRO 2018 software. Defect content investigations and light emission performances of NR and NF structured thin films were analyzed via a Horiba Jobin-Yvon Florog-550 photoluminescence (PL) system under 325 nm He : Cd laser excitation wavelength. Like XPS, the investigation of the origins of defect-related emissions was performed via Gaussian distributions through ORIGINPRO 2018. Emission spectra of thin film samples excited under corresponding laser energy were obtained under 1 nm slit number within 380–1000 nm wavelength range. EPR measurements were performed with a Bruker Benchtop EMX Nano spectrometer with an integrated referencing for g-factor calculation and an integrated spin counting unit. The microwave frequency of the resonator was 9.41 GHz, and all spectra were measured with 2 mW microwave power, 50 dB receiver gain, and 2 G modulation amplitude at room temperature. Powder samples

were inserted into spin-free quartz tubes (Qsil, Germany). EPR analyses were performed using nanostructures collected from CBD solution to obtain sufficient signals. As for the CIGS/In_2S_3-deposited ZnO samples were scratched from the surface to collect powder samples for EPR analysis. Due to the large surface area, we could obtain enough powder samples by scratching ZnONF/CIGS/In_2S_3. However, it was not possible to collect enough powder for ZnONR/CIGS/In_2S_3 owing to the small surface area of the NR structure.

C. PEC measurements

PEC performance of the photoelectrodes was explored using a Gamry Potentiostat in a three-electrode system. The fabricated thin films (1 cm^2 of active area) were used as the working, platinum wire as the counter, and Ag/AgCl as the reference electrodes in 0.35 M Na_2SO_3/0.25 M Na_2S (pH 12.5) electrolyte solution. The illumination condition was provided by a 100 W Xenon arc lamp with an AM 1.5G filter with 100 mW cm^{-2} intensity (1 sun illumination) at room temperature. IPCE data were collected using a monochromatic light source (FemtoTera, Femto-RD5) at 0V (vs Ag/AgCl) in the standard electrolyte. IMPS analysis of the photoelectrodes was performed under 382 nm modulated light with the AC amplitude of 200 mA and the frequency ranging from 0.1 Hz to 25 kHz (FemtoTera, Femto-RD25). All the related equations to evaluate efficiencies and electrochemical impedance spectroscopy results are given in the Supplemental Material [37].

III. RESULTS AND DISCUSSION

A. Morphological and structural properties of pristine ZnO thin films

ZnO NR and NF nanostructured thin films were employed as the substructures for spray pyrolyzed CIGS/In_2S_3 heterojunctions. To recognize the effects of these two morphologies, which are quite different from each other, on PEC performance, the morphological and structural properties of the pristine-ZnO thin film electrodes were thoroughly analyzed. Figures 1(a) and 1(b) depict the cross-sectional ESEM images of ZnO NF and NR, respectively. ZnO NF forms in the diameter range of ∼2–20 μm are recognized to be grown on the NW-like structures with smaller sizes (see Fig. S1(b) in the Supplemental Material [37]). The completely different nucleation-and-growth mechanism caused by the addition of nitric acid shifts the pH value of the reaction solution from slightly basic to acidic during the NF formation. On the other hand, a dense and uniform ZnO NR formation with an average length of ∼1.4 μm can be seen in Fig. 1(b). Additionally, as evidenced by the energy dispersive x-ray analysis, both ZnO structures have a higher atomic percentage of Zn, showing that both structures are formed with oxygen vacancies (V_o; see Fig. S2(a) in the Supplemental Material [37]). Figures 1(c) and 1(d) depict the high-resolution transmission electron microscopy (HRTEM) and transmission electron microscopy (TEM) (inset) images of ZnO NF and NR nanoparticles, respectively. The TEM image belonging to ZnO NF [Fig. 1(c), inset] confirms a neat flowerlike structure with ∼2.0 μm diameter while ZnO NR forms appear with an average diameter of 0.5 μm and length of 1.4 μm. The clear lattice fringe spacings (d spacing) of 0.24 and 0.26 nm confirm the hexagonal wurtzite structure of ABAB … stacking for NF and NR, respectively [Figs. 1(c) and 1(d)] [39–41]. Moreover, the grains and domains arising in the HRTEM image of ZnO NF indicate that the NF structure of ZnO is composed of small crystal grains, while no grains and domains could be observed in that of ZnO NR, demonstrating its consecutive crystallite orientations. Both XRD patterns of ZnO NR and NF thin films given in Figs. 1(e) and 1(f) indicate the hexagonal wurtzite structure of ZnO (JCPDS No. 36-1451) [12,42,43]. However, diffraction intensities of various crystal planes are observed, indicating various crystal orientations in the NF sample owing to the multidirectional nature of the leaves of the flowers. On the other hand, for the NR structure [Fig. 1(f)], the diffraction intensity of the (002) polar plane is dominant, as compared with the (100) nonpolar plane, indicating growth in the c-axis [44]. Additionally, strong reflexes, together with the HRTEM, indicate a high degree of crystallinity for NR structure.

Further structural investigation of pristine ZnO thin films was performed via Raman analysis [Fig. 2(a)]. The vibrational modes of the corresponding ZnO nanostructures were studied to detect structural disorders and defects. ZnO, having a wurtzite crystal structure, has four atoms in the unit cell with the symmetry space group of $C_{6v}^4(P_63mc)$ [45]. In group theory, the optic modes exist for a wurtzite structure according to the given equation $\Gamma_{opt} = A_1(TO) + 2B_1 + E_1(TO) + 2E_2$. Here, polar A_1 and E_1 modes split into transverse optical (A_1 TO and E_1 TO) and longitudinal optical (A_1 LO and E_1 LO) modes. Conversely, E_2 mode consists of low and high E_2 and relates with the vibration of heavy sublattice Zn and O atoms, respectively. Also, E_2 (high) is observed as the most intense peak at 439 cm^{-1} for both morphologies belonging to the intrinsic characteristic Raman active mode of wurtzite hexagonal ZnO. This peak is much more intense for NR morphology. Additionally, the broadband detected at ∼584 cm^{-1} fits A_1(LO) and is regarded as crystal structural disorders, such as Zn interstitial and oxygen vacancies. Further, E_1(LO) mode is present at ∼1155 cm^{-1}, while the A_1(TO) band appears at 331 cm^{-1}. Since the E_1(LO) mode is also linked with the defect structure, which could include oxygen vacancies and interstitial Zn, both Raman spectra exhibited defect and oxygen vacancy in crystal structures [46].

XAFS spectroscopy results were collected for the investigation of structural disorder around Zn atoms caused by morphological variation. The K-edge absorption signals of the Zn atom, which occur by the transition of 1s core electron to the final state (unoccupied 4p level) can be seen in Fig. 2(b). The absorption edge for both NR and NF begins to rise at ∼9660 eV and has a maximum of 9668 eV (denoted as A and B). This main peak can be attributed to the Zn^{2+} dipole that allowed electron transitions from 1s to the 3d final states [47]. It has been previously reported that the intensity of this peak could be increased by the local atomic configuration lacking centrosymmetry [48]. The broadening in the main peak at 9668 eV NR might be the result of eliminating the heat treatment (calcination step) on the NR structure after CBD growth. On the contrary, the NF thin film was calcinated at 300 °C after CBD growth to convert loosely bound $Zn(OH)_2$ to ZnO, which also changes in bond lengths. Thus, the

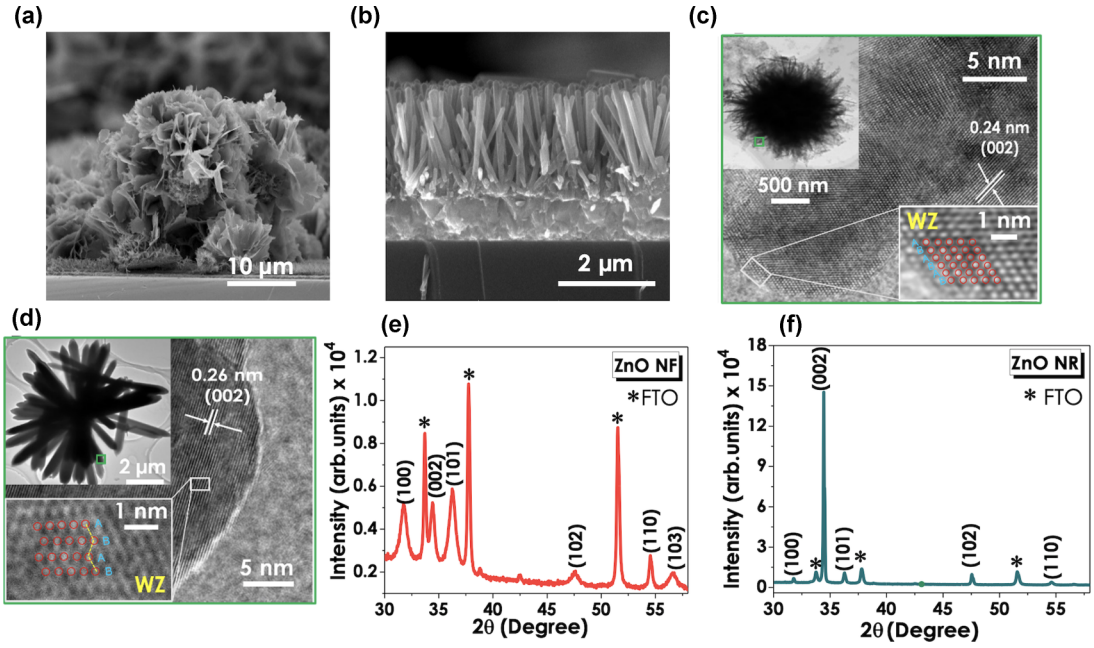

FIG. 1. Cross-sectional environmental scanning electron microscopy (ESEM) images for (a) ZnO nanoflower (NF) and (b) ZnO nanorod (NR). High-resolution transmission electron microscopy (HRTEM) image with transmission electron microscopy (TEM) (inset) of (c) ZnO NF and (d) ZnO NR. X-ray diffraction (XRD) patterns of (e) ZnO NF, and (f) ZnO NR thin films.

signals above the absorption edge at 9680 eV which are linked to the scattering contribution from high coordination shells show distinction [48]. The slight shift in *K*-edge absorption obtained for the energies >9670 eV could be due to the ionic Zn atoms resulting from electron share during the bonding interactions [49]. The effect of heat treatment on XAFS spectra was revealed for ZnO for causing a decrease in intensity of the peaks consistent with the previously reported study [48].

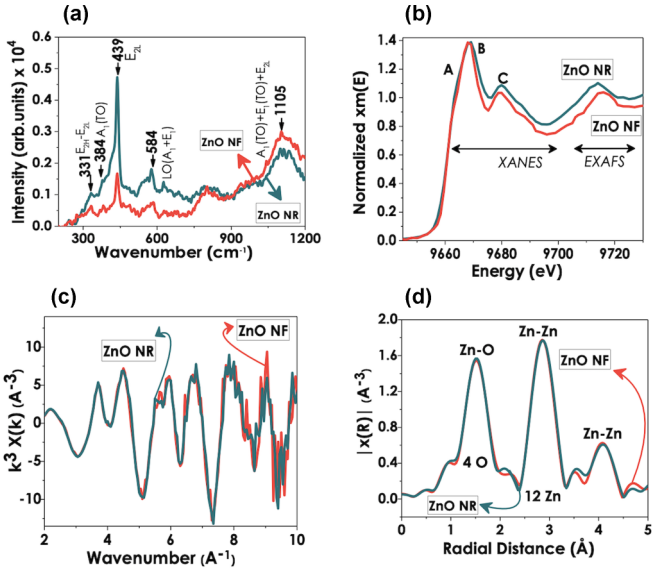

FIG. 2. (a) Room-temperature Raman shifts obtained under 525 nm line excitation, (b) x-ray absorption fine structure (XAFS), (c) x-ray absorption near-edge spectroscopy (XANES), and (d) extended x-ray absorption fine structure (EXAFS) analysis results obtained from ZnO NR and NF samples.

Despite the slight shift, it is possible to conclude that, in XANES, the intensity of the white line (denoted as A and B) related to charge-transfer effects is almost the same for both structures. The data for the extended EXAFS analysis obtained from the measured XAFS spectra by using ATHENA and ARTEMIS software are given in Fig. 2(c). Both NR and NF thin films display similar signal behavior. The radial distribution function of the EXAFS χ data in Fig. 2(d) shows that bond lengths of O and Zn in both wurtzite structures are quite similar as 0.15 and 0.29 nm for Zn-O and Zn-Zn bonds, respectively. As a result, the x-ray absorption measurements indicated that both morphologies of ZnO thin films have similar electronic structures and bond lengths.

The elemental composition and detailed defect content inspection of ZnO thin films were performed via XPS, PL, and EPR analyses. Previously, it has been reported that the elemental composition and the defect properties of the ZnO-based photoelectrodes strongly affect the PEC and photocatalytic performances [50,51]. XPS data, which served to elaborate the elemental composition of pristine ZnO thin films, are given in Fig. 3. The survey spectra of individual ZnO NR and NF films show the presence of characteristic Zn and O peaks [Fig. 3(a)]. The investigation of the chemical state of each film was performed via analyzing the Gaussian distribution of their O1s peaks, separately. ZnO NR, which was analyzed in our previous study, comprised a significant shoulder formation at ~530.8 eV; the O1s spectrum was fitted into three Gaussian peaks marked as O1, O2, and O3 [52]. Here, considering the presence of an apparent shoulder, a threefold deconvolution was preferred as a better fit. The peak located at 530 eV belongs to the oxygen ions of the wurtzite ZnO structure whose intensity denotes the number of oxygen atoms in the completely oxidized surrounding [53]. The secondary peak appearing at ~531 eV represents the

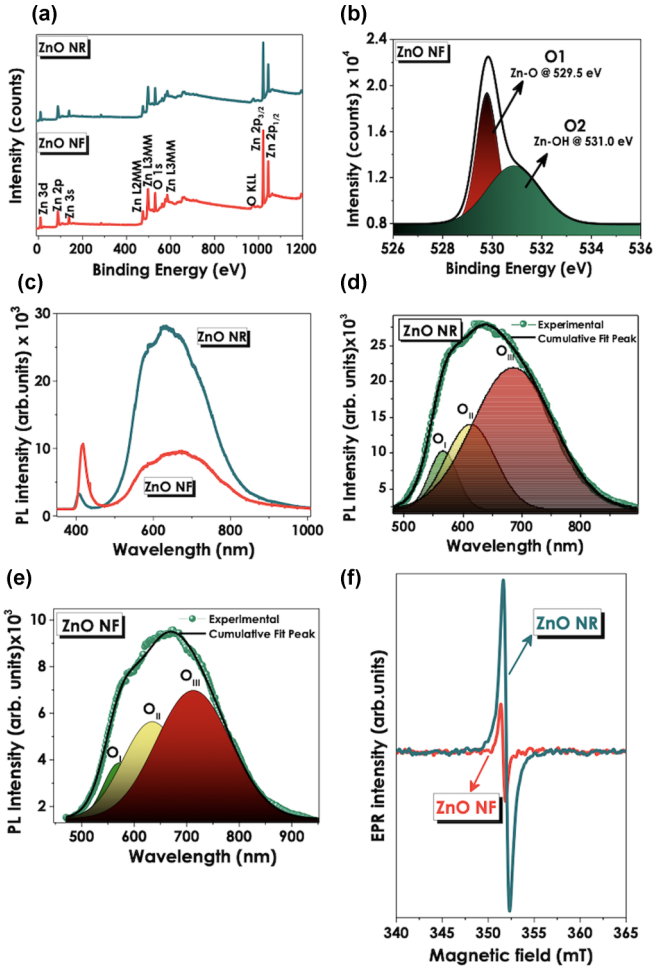

FIG. 3. (a) X-ray photoelectron spectroscopy (XPS) survey spectra and (b) deconvoluted O1s curve for ZnO nanoflower (NF). (c) Photoluminescence (PL) spectra of ZnO nanorod (NR) and NF thin film photoelectrodes. Deconvoluted PL curves for the ZnO (d) NR and (e) NF defect identification. (f) Electron paramagnetic resonance (EPR) spectra of ZnO NR and NF nanoparticles.

oxygen ions residing in the oxygen-deficient parts of the ZnO matrix. Hence, the intensity of this peak gives a clue about the amount of oxygen vacancy defects within the structure. The latter peak (O3), appearing at higher binding energies (532 eV), is ascribed to loosely bound, dissociated oxygen or −OH species. The O1s spectrum of the ZnO NF structure, on the other hand, was successfully deconvoluted into two fitting Gaussian peaks marked as O1 (530 eV) and O2 (531 eV) [Fig. 3(b)] [9,54]. Here, the low binding energy peak stands for the O^{2-} ions of Zn-O bonding, while the higher binding energy peak represents the intensity of oxygen-deficient regions [50,55]. Studies interpret interpret this kind of a two-peak fitting as a relatively higher oxygen content due to having more O_2 molecules adsorbed to oxygen vacancy regions [56,57]. Moreover, in contrast to NR structures that are not exposed to a high-temperature calcination step, after their CBD growth, NF thin films are annealed at 300 °C. This annealing step ensures the conversion of loosely bound −OH species into ZnO, therefore quenching the origin of the third deconvolution peak. To interpret the evaluated data, a comparison was established between the intensities of deconvoluted O1s peaks (O1 and O2). This way, a clear image of the oxygen vacancy concentration within both structures may be obtained. Hence, the ratio of O2/O1 calculated for both nanostructures was evaluated as ∼1.09 for NF and ∼0.98 for NR, showing a more dominant presence of oxygen vacancy defects within NF formations.

PL was conducted as an *a fortiori* analysis to better interpret the defect content of ZnO NF and NR, individually. The given technique also served as the detection of emission ranges of both nanostructures. Analyzing the overall PL spectra of ZnO nanostructures given in Fig. 3(c), two characteristic peaks at wavelengths $\geqslant$380 and $\geqslant$550 nm are observed. The primary peak appearing at the UV region represents the excitonic emissions due to the presence of Coulombic forces in the ZnO lattice. The next emission peak generating in the yellow-green region is caused by the defects present in the ZnO nanostructures. For the detailed analyses of the defect content of both NR and NF structures, each individual PL peak at the yellow-green region was deconvoluted into three Gaussian bands [Figs. 3(d) and 3(e)], and detailed fitting data are given in Table S1 in the Supplemental Material [37]. These corresponding Gaussian bands are labeled as (i) O_I for the 530–580 nm range, (II) O_{II} for the 580–640 nm range, and (III) O_{III} for 640–800 nm range. According to the previous comments on deconvoluted ZnO Gaussian bands reported in the literature, peaks located within the 530–640 nm wavelength range of O_I and O_{II} correspond to singly and doubly charged oxygen vacancies denoted as V_o^+ and V_o^{++}, respectively [58–60]. The latter Gaussian band residing at the 640–800 nm region was found to represent zinc vacancies (V_{Zn}) or oxygen interstitials (O_i). Examining both nanostructures, it can be observed that, for NF morphology, the total area remaining under the bands representing the V_o (i.e., $O_I + O_{II}$) exceeds the area representing other types of defects (O_{III}) by 1.3-fold. The situation is the opposite for NR structures containing higher amounts of V_{Zn}/O_i than the total amount of oxygen vacancies [61,62]. Hence, a comparatively more V_o-rich defect content of ZnO NF was confirmed via PL and XPS techniques.

Further investigation of the defects in pristine ZnO nanostructures was performed via EPR. The EPR analysis was performed on the powder samples which were collected from CBD reaction solution to obtain reliable signals. A typical defect signal observed for both pristine ZnO nanostructures is generated due to singly ionized oxygen vacancies, as supported by the XPS and PL. These vacancies are the major defect centers in ZnO, whereas ionized zinc vacancies, oxygen, and zinc interstitials also contribute to this EPR signal as a minor amount of defect centers. It is also known that the theoretical first-principles calculation via density functional theory suggests the lowest formation energy for the oxygen vacancy defect center. In general, the bounded state defects on the bulk volume give g-factors ∼1.96. As can be seen from Fig. 3(f), there is a slight difference in g-factors between NF and NR structures. This is closely related to spin-orbit interaction, morphology, and the synthesis route. All three facts have an impact on the g-factor, eventually affecting the local configuration and concentration of vacancies. This results in a shift in the g-factor and the intensity of the EPR signal. The ZnO NR powder shows a stronger EPR signal than that of

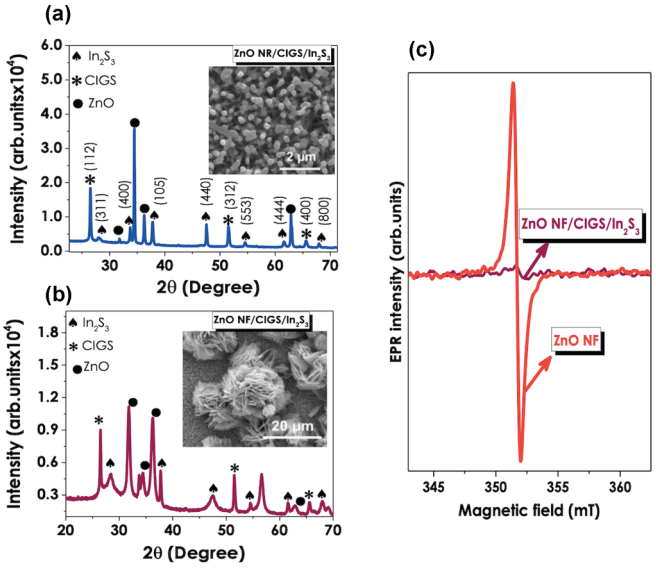

FIG. 4. X-ray diffraction (XRD) patterns of the thin film photoanodes with inset environmental scanning electron microscopy (ESEM) images of (a) ZnO nanorod (NR) and (b) nanoflower (NF) thin films after introducing CIGS/In_2S_3 layers. (c) Electron paramagnetic resonance (EPR) spectra of pristine ZnO NF and ZnO NF/CIGS/In_2S_3.

NF, which was caused by trapped electrons on the surface. Oxygen vacancy on the surface inclines to adsorb atmospheric O_2 molecules and form reduced O_2^- to generate an intense EPR signal [63].

B. Structural and optical properties of ZnO/CIGS/In_2S_3 thin films

The XRD patterns of the ZnO-based thin films after introducing CIGS/In_2S_3 heterojunctions [Figs. 4(a) and 4(b)] indicate the presence of characteristic chalcopyrite CIGS (JCPDS No. 35-1102) and β-In_2S_3 (JCPDS No. 65-0459) signals for ZnO NR and NF, respectively [30,64]. The characteristic signals belonging to the FTO substrate observed in Figs. 1(e) and 1(f) disappeared with the suppression of the additional peaks of the CIGS/In_2S_3 heterojunction. In addition, we confirmed that the morphologies of ZnO thin films remain almost unchanged after spray pyrolyzing the CIGS/In_2S_3 heterojunction, with the ESEM images given as insets in Figs. 4(a) and 4(b). The results of the EDAX analysis obtained before and after CIGS/In_2S_3 heterojunction deposition are displayed in Figs. S2(a) and S2(b) in the Supplemental Material [37]. Figure S2(a) in the Supplemental Material [37] displays the Zn and O contents for both ZnO nanostructures, indicating the higher content of Zn. After deposition of CIGS/ In_2S_3, Cu, In, Ga, and S contents can be observed in Fig. S2(b) in the Supplemental Material [37]. The higher contents of In and S were observed due to the higher pass number of In_2S_3 deposition during the spray pyrolysis process.

The change in defect content after introducing the CIGS/ In_2S_3 layer was investigated via EPR analysis. As mentioned before, the powder sample for ZnO/CIGS/In_2S_3 which was obtained from the thin film surface was preferable to conduct a more reliable EPR analysis. Thus, the surface of the thin film was scratched to collect powder samples for EPR analysis [Fig. 4(c)]. Due to the large surface area, we could obtain enough powder samples by scratching ZnONF/CIGS/In_2S_3. However, it was not possible to collect enough powder for ZnONR/CIGS/In_2S_3 owing to the small surface area of NR. In general, defects like vacancies and interstitials are mostly diamagnetic. However, ZnO can trap electrons that ionize the defects, and these singly or doubly ionized defects become paramagnetically active and detectable by EPR. A typical defect signal observed for both pristine ZnO nanostructures [Fig. 3(f)] is generated due to singly ionized oxygen vacancies. These vacancies are the major defect centers in ZnO, whereas ionized zinc vacancies, oxygen, and zinc interstitials also contribute to this EPR signal as a minor amount of defect centers. In Fig. 4(c), the change in defect centers of NFs are tested by scratching the thin film from the surface. Once the NFs form the composite together with CIGS/In_2S_3, the defect concentration reduces dramatically. Such a reduction of defects shows that CIGS/In_2S_3 layers play the role of surface passivating agents, therefore positively affecting the PEC performance, as discussed later.

The optical absorbance of the ZnO/CIGS/In_2S_3 thin film photoelectrodes is summarized in Fig. 5(a), indicating that the absorbance in the visible region is comparatively better for ZnO NF thin film photoanode owing to the multiple reflections and light scattering, which later supports the superior PEC performance compared with that of ZnO NR. Moreover, both ZnO NR and NF photoanodes exhibited an effective absorption edge ~382 nm. The absorbance behavior of the inversely configurated thin films exhibited a wide range of UV-Vis absorption due to the CIGS/In_2S_3 layers. It was also noted that the ZnO NF/CIGS/In_2S_3 thin film has comparatively better absorbance in the entire visible spectrum, possibly due to multiple reflections and scattering. Figure 5(b) displays the steady-state PL spectra for the thin film for ZnO/CIGS/In_2S_3 photoelectrodes. Both PL emissions at ~420 and ~690 nm which are observed for ZnO NR and NF thin films appear with a quenching effect after introducing CIGS/In_2S_3 layers due to the enhanced charge separation rendered by the CIGS/In_2S_3 decoration. It is also noted that the emission at ~560 nm, which is observed for the ZnO NR/CIGS/In_2S_3 photoelectrode, appears possibly due to radiative recombination between the V_S and V_{In} defect levels of In_2S_3, which has been reported for spray pyrolyzed In_2S_3 [65,66]. In contrast to ZnO NR, ZnO NF/CIGS/In_2S_3 thin film does not exhibit this sharp defect-based emission, possibly due to the suppression of PL emission resulting from V_o^+ of the NF morphology explained in Fig. 3(e). Figures 4(c)–4(g) display the XPS survey and high-resolution XPS profiles of Cu 2p, In 3d, Ga 3d, and S 2p regions of ZnO/CIGS/In_2S_3 thin films. In the In 3d region [Fig. 5(d)], two characteristic signals, observed at ~444.5 eV (In $3d_{5/2}$) and ~452.1 eV (In $3d_{3/2}$), are in good agreement with In^{+3}. The two signals residing at higher (951.8 eV) and lower BE (931.9 eV) in the Cu 2p region having 19.9 eV of the spin-orbit splitting is evidence of the Cu^+ ion [Fig. 5(e)] [67].

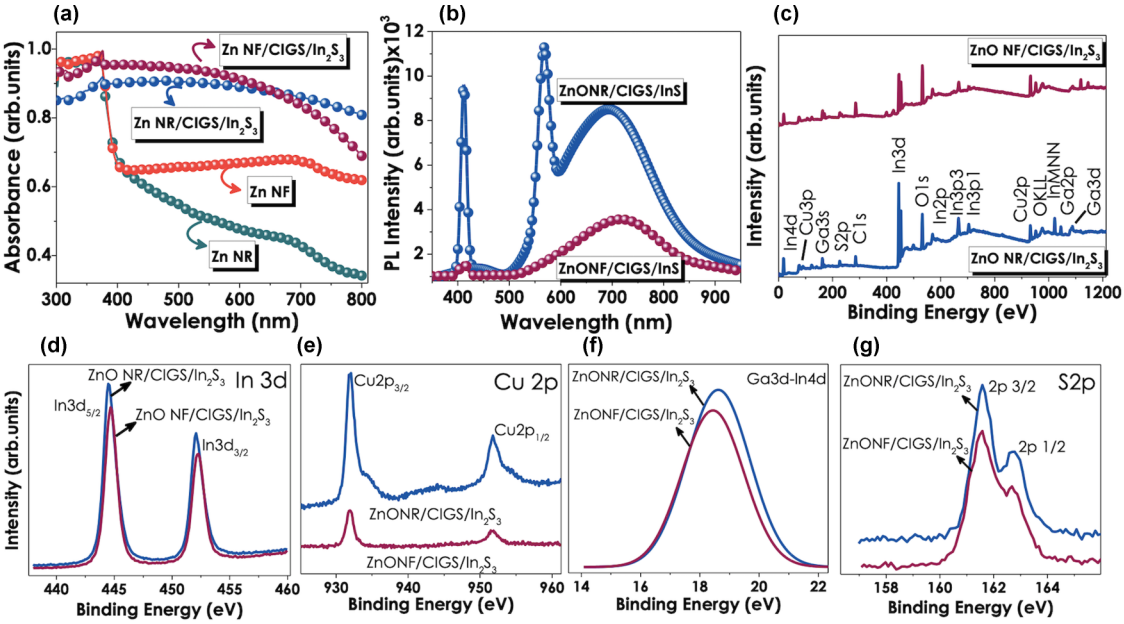

FIG. 5. (a) Ultraviolet (UV)-visible (Vis) absorption spectra, (b) photoluminescence (PL) curves, (c) x-ray photoelectron spectroscopy (XPS) survey, and high-resolution XPS profiles of (d) In 3*d*, (e) Cu 2*p*, (f) Ga 3*d*, and (g) S 2*p* regions of ZnO/CIGS/In_2S_3 thin films.

C. Photo- and electrochemical performances of ZnO-based thin films

The photocurrent density (J) vs applied potential (V) curves acquired by linear sweep voltammetry measurement are given in Figs. 6(a) and 6(b). Despite the comparatively low photocurrent density (~0.3 mA cm^{-2} at 0 V vs Ag/AgCl), pristine ZnO photoelectrodes are still quite favorable for water splitting reaction (see Fig. S3(a) in the Supplemental Material [37]). Chronoamperometric tests performed under chopped light at 0 V (vs Ag/AgCl) indicated that 74% of the initial J remains for NF photoelectrodes after 2 h (see Fig. S3(b) in the Supplemental Material [37]), while 57% of the initial J remains for ZnO NR. Additionally, direct photocatalytic hydrogen production from water indicates significantly improved activity over ZnO NF. The initial H_2-evolution rate reaches 276.6 μmol h^{-1} g^{-1} over ZnO NF, which is ~30 times higher than that of ZnO NR (see Fig. S3(c) in the Supplemental Material [37]). This extreme enhancement in photocatalytic performance of ZnO NF would be the result of a higher surface-to-volume ratio that contributes to the effective light absorption and quenched PL given in Figs. 5(a) and 5(b). Indeed, the efficiency of the photogenerated charge carrier density and recombination of the electron-hole pair can be revealed by PL spectra since there is a direct relationship between PL intensity and photocatalytic efficiency [68,69]. On the other hand, CIGS is known as a strong light absorber material that can boost light absorption, resulting in high photocurrent density. However, the lack of favorable energetic alignment of the bare CIGS with the electrolyte solution leading to inefficient charge separation of carriers results in low PEC performance. Additionally, copper-based chalcopyrites suffer from severe photocorrosion. Therefore, the deposition of the In_2S_3 buffer layer on top of CIGS supplied a better alignment between the photoelectrodes and electrolyte solution. ZnO NF/CIGS/In_2S_3 photoelectrodes generated photocurrent density of 5.5 mA cm^{-2} at 0.4 V (vs Ag/AgCl) under 1 sun illumination [Fig. 6(a)]. On the other hand, a record photocurrent density generation of 30.0 mA cm^{-2} at 0.4 V (vs Ag/AgCl) was achieved from the photoelectrode with ZnO NR/CIGS/In_2S_3 configuration [Fig. 6(b)]. However, a significant increase in dark current was also noticed with increasing the potential, which based on the previously reported works, has been attributed to the electro-/photocorrosion of S^{2-} and Cu^{+} [70]. It is important to note that we have completely overcome the dark current

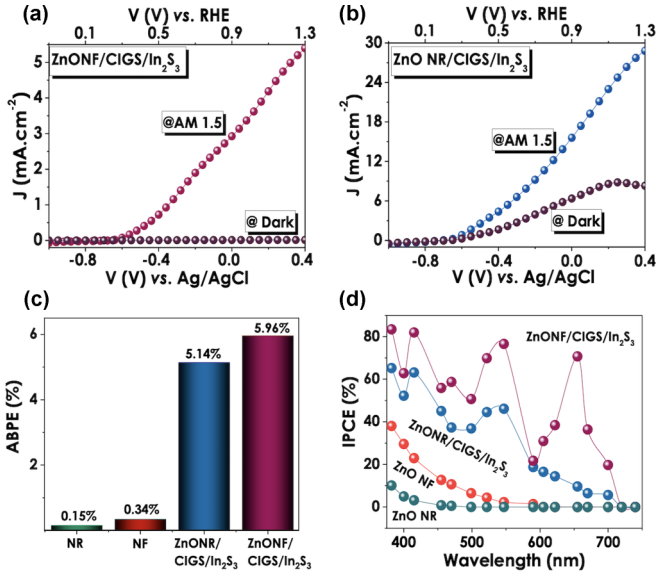

FIG. 6. J-V curves of the inverted (a) ZnO nanoflower (NF)/CIGS/In_2S_3 and (b) ZnO nanorod (NR)/CIGS/In_2S_3 photoelectrodes. (c) Applied bias photon-to-current efficiency (ABPE%) and (d) incident photon-current efficiency (IPCE%) obtained for pristine and CIGS/In_2S_3 deposited ZnO nanostructures.

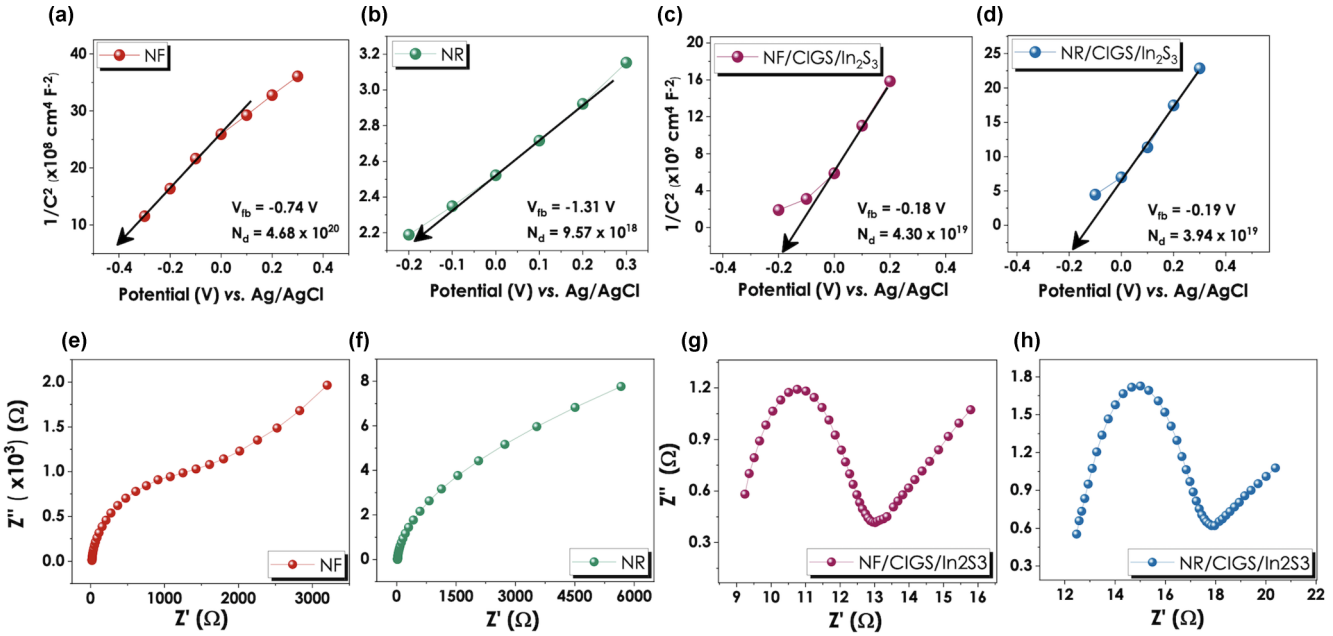

FIG. 7. Mott-Schottky plots obtained for (a) ZnO nanoflower (NF), (b) ZnO nanorod (NR), (c) ZnO NF/CIGS/In_2S_3, and (d) ZnO NR/CIGS/In_2S_3 thin films with corresponding V_{fb} and N_d values. Nyquist plot of (e) ZnO NF, (f) ZnO NR, (g) ZnO NF/CIGS/In_2S_3, and (h) ZnO NR/CIGS/In_2S_3.

issue by using the three-dimensional (3D) ZnO NF electrode beneath the CIGS/In_2S_3 layer [Fig. 6(a)]. Additionally, advantages of the inverted structure of the semiconductor layers for solar cell applications have been reported [70]. Basically, sandwiching the small bandgap absorber in between large bandgap semiconductors increases the conversion efficiency due to the enhancement in the absorption of the incident light, charge generation, and collection in the active layer [70]. The stability test which was performed at 0 V (vs Ag/AgCl) exhibited a rapid decline in photocurrent within the first four cycles for both photoelectrodes, indicating the degradation of the CIGS/In_2S_3 layers with time (see Fig. S3(e) in the Supplemental Material [37]). However, after the fourth cycle, photocurrent density stayed almost constant. Additionally, electrodes based on ZnO NF performed with better stability than ZnO NR. The PEC efficiency evaluation equations of the photoelectrodes are given as Eqs. (S1)–(S3) in the Supplemental Material [37]. The applied bias photon-to-current efficiency (ABPE%) comparison data displayed in Figs. 4(c) and S3(d) and S3(f) in the Supplemental Material [37], indicate that the photoelectrodes with the CIGS/In_2S_3 layer coating were boosted to 5.14 and 5.96% for ZnO NR and NF, respectively. The lower ABPE was observed for ZnO NR/CIGS/In_2S_3 configurated photoelectrode due to the high dark current generation, despite very high photocurrent generation by this photoelectrode, as shown in Fig. 6(b). Figure 6(d) displays the IPCE% of all photoelectrodes before and after decoration of the CIGS/In_2S_3 layers. The ZnO NF photoelectrode exhibited four times higher IPCE than that of ZnO NR-based photoelectrode, supporting the optical spectroscopy measurements. Consequently, the maximum IPCE% value was evaluated as 83% at 382 nm illumination for the ZnO NF/CIGS/In_2S_3 photoelectrode. We also note that each layer of the photoelectrodes enhanced the IPCE% on their individual active light absorption wavelengths, resulting in a fluctuation in the overall IPCE measurement. All equations used in evaluating ABPE% and IPCE% measurements with related conversions are specified in the Supplemental Material [37].

Electrochemical impedance spectroscopy (EIS) was used as a nondestructive analysis for the characterization of the interaction between semiconductor electrodes and electrolyte solution. Additionally, EIS measurements were conducted as as a *fortiori* analysis to validate the improvement in photoelectrode-electrolyte interfaces after CIGS/In_2S_3 deposition. Once the photoanode is submerged into the electrolyte, significant changes occur in both the intrinsic and electrical properties of the materials. Mott-Schottky analyses were performed to evaluate the intrinsic parameters, which are the flat band potential (V_{fb}) and density of charge carriers (N_d), of both pristine and CIGS/In_2S_3-deposited ZnO thin films [Figs. 7(a)–7(d)]. The well-known details of the flat band calculation and the charge density are given in the Supplemental Material [37]. The obtained results show strongly negative V_{fb} values for pristine ZnO NR and NF films with a significant positive shift after CIGS/In_2S_3 deposition. Hankin *et al.* [71] report that the reason for this sharp negativity may arise due to the intense doping of *n*-type semiconductors. In other words, taking a closer look at N_d values of both pristine and CIGS/In_2S_3-deposited ZnO NF, a distinguishable decrease in charge carrier concentration can be observed after the deposition step. This shows that, in their bare forms, ZnO NFs act as strongly doped semiconductor materials ($N_d =\sim 10^{20}$ cm^{-3}), generating more negative V_{fb} values, while after the incorporation of CIGS/In_2S_3 layers, V_{fb} values increase, consequently resulting in a decrease in $N_d (\sim 10^{19})$. Moreover, it is highly important to note that it is specifically the positive shift of V_{fb} that strongly increases the

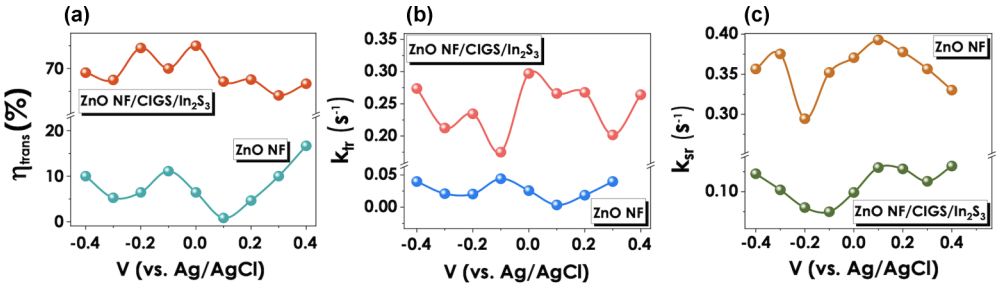

FIG. 8. (a) Charge transfer efficiency, (b) charge transfer rate, and (c) surface recombination rates of ZnO nanoflower (NF) and ZnO NF/CIGS/In_2S_3 composite structures calculated using intensity-modulated photocurrent spectroscopy (IMPS) measurements.

charge transfer kinetics, which is in good agreement with the increase in IPCE% and *J-V* performances after CIGS/In_2S_3 deposition on ZnO NFs [72]. A different situation applies for ZnO NRs, which possess a strongly negative V_{fb} value but, on the contrary, have a much smaller charge carrier concentration ($N_d =\sim 10^{18}$ cm^{-3}). Przezdziecka *et al.* [73] report that the low N_d value in ZnO thin films grown under low reaction temperatures (<100 °C) is attributed to a higher ratio of oxygen to zinc. This statement agrees with PL responses obtained for ZnO NRs showing an increased amount of O_i. Analyzing the N_d value for ZnO NR/CIGS/In_2S_3 thin films, a significant positive shift in the V_{fb} value confirms an improved charge transfer kinetics after the chalcopyrite/chalcogenide deposition. However, for these thin films, the N_d value also increases from $\sim 10^{18}$ to $\sim 10^{19}$, which is assumed to be affected by the postannealing step of ZnO NRs during consecutive CIGS and In_2S_3 depositions.

Nyquist plots given in Figs. 7(e)–7(h) were used for the evaluation of changes in electrochemical impedances of ZnO thin films before and after CIGS/In_2S_3 deposition. The obtained plots were fitted into suitable equivalent circuits (ECs) containing basic circuit elements such as resistors and capacitors. The standard Randles EC with the addition of the Warburg element was selected as the suitable circuit for the obtained plots where series resistance (R_S), representing the solution resistance and capacitor (C), are connected in parallel to charge transfer resistance (R_{CT}), symbolizing the resistance between semiconductor and electrolyte solution. [9] The detailed elaboration of each circuit element specified in the tabulated form of Figs. 7(e)–7(h) shows approximately close R_S values for all four photoelectrodes (see Eqs. (S4) and (S5) and Table S2 in the Supplemental Material [37]). However, a distinguishable decrease can still be observed for R_S values because of CIGS/In_2S_3 incorporation. Moreover, higher R_{CT} was evaluated for pristine ZnO NR, proving a more resistive charge transfer mechanism between electrodes and electrolyte solution. On the other hand, a very strong R_{CT} drop can be reported for the CIGS/In_2S_3-deposited thin films. These results, being in remarkably good agreement with the obtained performance values, evidence that the increasing current densities and efficiencies are strongly connected to the improved charge transfer kinetics because of the incorporation of inverted configuration. Thus, the conducted EIS analyses were used as additional crosscheck characterization proving the occurrence of an appreciable change in electrical properties of ZnO thin films after CIGS/In_2S_3 deposition.

Since the PEC performances of the pristine and CIGS/In_2S_3-heterojunction-decorated ZnO NF thin film photoelectrodes were found to be more efficient, we focused on the investigation of the charge transport and recombination rates of these photoelectrodes in detail. IMPS is a very powerful technique to understand the charge transport and recombination rates between the photoactive electrode and electrolyte solution [74,75]. Thus, IMPS was used to determine the charge transport and recombination rates between the ZnO NF electrodes and electrolyte solution. The schematic illustration of the processes at an illuminated *n*-type semiconductor/electrolyte solution interface is given in Fig. S4(a) in the Supplemental Material [37]. The transfer function (H) is calculated by dividing the modulated photocurrent by the modulated photon flux. Here, H is also defined as the frequency-dependent external quantum efficiency, which is used to determine PEC kinetics and mechanisms. Generally, charge transfer and surface recombination mechanisms are considered. The rates of charge transfer (k_{tr}) and surface recombination (k_{sr}) can be calculated by using the Im H vs Re H plot, as shown in Fig. S4(b) in the Supplemental Material [37]. The charge transfer efficiency (η_{trans}) can be calculated by dividing the high-frequency intercept to the low intercept of the Im H vs Re H plot, as described in Eq. (S6) in the Supplemental Material [37]. The Nyquist plot of Im H vs Re H of the pristine and CIGS/In_2S_3-deposited ZnO NF under 0 V applied bias (vs Ag/AgCl), 382 nm modulated light with the AC amplitude of 200 mA, and the frequency ranging from 0.1 Hz to 25 kHz, can be seen in Figs. S4(c) and S4(d) in the Supplemental Material [37], respectively. The charge transfer efficiency (η_{trans}) of the ZnO NF electrode enhanced by more than sevenfold after CIGS/In_2S_3 decoration and reached 75% at 0 V bias (vs Ag/AgCl) [Fig. 8(a)]. Additionally, IMPS results prove that the CIGS/In_2S_3 decoration increased the charged transfer rate while the surface recombination kinetic is lowered [Figs. 4(b) and 4(c)]. As a result, it can be concluded that spray pyrolysis of CIGS/In_2S_3 reduced the surface defects of ZnO NF electrodes. As previously evidenced, the applied heat during the pyrolysis process, chlorine-based metal salts used in the spray solution, and electron transfer from a more conductive layer through the ZnO surface can be reasons for the reduction of the concentration of oxygen vacancies [33].

Table I compares the performances obtained from this paper with the related Cu-based chalcopyrite photoelectrodes reported in the literature recently. As can be seen from

TABLE I. Comparison of the literature reporting ternary sulfide photoanodes with cadmium- and cadmium-free configurations. NA = not available.

Photoanode	Electrolyte	J_{photo} (mA cm^{-2})	ABPE%	IPCE%	Ref.
ZnONR/CIGS/In_2S_3	Na_2S/Na_2SO_3	30 (@1.3 V vs RHE)[a]	5.14	65 at 0 V (Ag/AgCl)	This paper
ZnONF/CIGS/In_2S_3	Na_2S/Na_2SO_3	5.5 (@1.3 V vs RHE)	5.96	83 at 0 V (Ag/AgCl)	This paper
ZnONW/In_2S_3/CIS	Na_2S/Na_2SO_3	2.4 (@0V vs RHE)	NA	60 at 0.4 V (Ag/AgCl)	[76]
CIS/$ZnIn_2S_4$	Na_2SO_4	0.7 (@1.23 V vs RHE)	0.08	NA	[77]
$CdIn_2S_3$	Na_2S/Na_2SO_3	5.7 (@1.23 V vs RHE)	2.49	60 at 0.6 V (RHE)	[78]
CISe/Al_2O_3	Na_2SO_4/KOH	12.7 (@1.23 V vs RHE)	NA	75 at 1.3 V (RHE)	[79]
ZnONW/Ag/CIS	Na_2SO_3/Na_2S	0.07(@1.23 V vs RHE)	0.05	NA	[80]
ZnONW/CdS/CIS	Na_2SO_3/Na_2S	13.8 (@0.3 V vs SCE)[b]	NA	NA	[81]

[a]RHE is the reversible hydrogen electrode.
[b]SCE is the standard calomel electrode.

this table, CIGS and CIS photoelectrodes can act both as photoanode and photocathode. Inverted configuration of ZnO NR/CIGS/In_2S_3 and NF/CIGS/In_2S_3 photoanodes proved to be highly efficient compared with the photoelectrodes fabricated with high-cost noble metals and/or time-consuming fabrication processes.

D. Electric field distribution of ZnO-based thin film photoelectrodes

Finally, the electric field distribution of CIGS/In_2S_3-decorated ZnO NR and NF structures were simulated by COMSOL Multiphysics (License No.: 17077178). Simulation of electric field distribution in both pristine and CIGS/In_2S_3-decorated ZnO nanostructures was performed via Wave Optics/Electromagnetic Waves Module. Modeling in NR structures was performed via frequency domain interface, while beam envelopes were applied on more complex NF geometries. The given module utilizes the finite element method (FEM) to solve the frequency domain form of Maxwell's equations. FEM can be described as a "numerical method" which provides an approximate solution for a boundary value problem. In more detail, a FEM converts the differential equations into a much simpler linear system of equations. The solution of both interfaces is based on the solution of modified Maxwell's equations:

$$\nabla x\left(\mu_r^{-1}\nabla x\mathbf{E}\right) - \frac{\omega^2}{c_0^2}\left(\epsilon_r - \frac{i\sigma}{\omega\epsilon_0}\right)\mathbf{E} = 0. \quad (1)$$

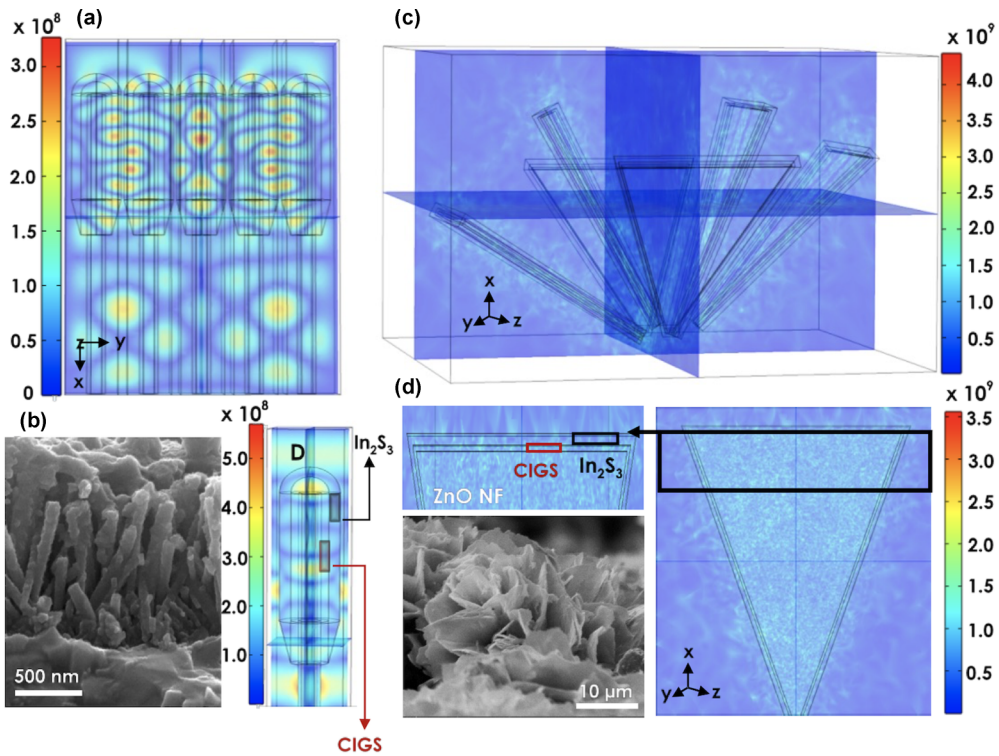

FIG. 9. The electric field distribution model of (a) bundle and (b) single ZnO nanorod (NR)/CIGS/In_2S_3 with its corresponding cross-sectional scanning electron microscopy (SEM) image. Electric field distribution model of (c) bundle, and (d) single-petal ZnO nanoflower (NF)/CIGS/In_2S_3 with a zoomed view representing the upper chalcopyrite-chalcogenide layers and a cross-sectional SEM image.

Figures 9(a)–9(d) and S5 in the Supplemental Material [37] depict the distribution of the magnitude of the electric field, as indicated by the color scale, for CIGS and In_2S_3-decorated single and bundle ZnO NR and ZnO NF, respectively. The required optical functions (refractive index n and extinction coefficient κ) of the CIGS and In_2S_3-deposited glass substrates were calculated from spectroscopic ellipsometry measurements (see Fig. S6 in the Supplemental Material [37]). As can be seen from these figures, ZnO NF samples present a higher magnitude of the electric field distribution than the ZnO NR, most probably due to the greater light-scattering obtained for the NF structure. Similarly, Shi *et al.* [82] reported that the tungsten trioxide helix nanostructures resulted in higher electric field intensity with more complex distribution than other structures like NRs due to the greater light-scattering cross-section. Additionally, ZnO NR arrays decorated with CIGS/In_2S_3 had a more complex electric field distribution than that of single NRs. On the other hand, ZnO NF structures had a more homogenous distribution with a higher amplitude, consistent with the higher charge transfer rates calculated for CIGS/In_2S_3-decorated ZnO NFs using IMPS measurements.

IV. CONCLUSIONS

The enhancement in PEC performance by increasing the surface-to-volume ratio of ZnO nanostructures that results in a more efficient light absorption has been presented. Accordingly, spray pyrolyzed CIGS/In_2S_3 heterojunctions on ZnO NR and NF nanostructures have been introduced as light absorber materials acting simultaneously as a defect passivation layer. PEC performance outcomes have shown that the heterojunction photoelectrodes are extremely efficient, generating very high photocurrent densities of 30.0 and 5.5 mA cm^{-2} (at 0.4 V vs Ag/AgCl) for NR and NF morphologies, respectively. However, the increase in dark current has lowered the photoconversion efficiency for ZnO NR/CIGS/In_2S_3 photoelectrodes. On the other hand, almost zero current density under dark conditions has been observed for ZnO NF, resulting in remarkably high IPCE and ABPE of 83 and 5.96%, respectively. EPR analysis, showing a drastic diminishment in the defect concentration with the decoration of a CIGS/In_2S_3 heterojunction on ZnO NF, explains the outstanding enhancement in PEC performance. In addition, IMPS outcomes have proven that the charge transfer rate increased while the surface recombination kinetic has been lowered with CIGS/In_2S_3 decoration. Numerical calculations of the pristine ZnO nanostructured thin films showed that NF exhibited a higher magnitude of the electric field distribution than ZnO NR, supporting the experimental outcomes. More complex electric field distribution has been observed after the addition of the CIGS/In_2S_3 layer on NR. Consequently, with this paper, we have proven that the CIGS/In_2S_3 mixed sensitization of the ZnO nanostructured thin films not only enhances the light absorption but also improves the charge transfer rate and surface defect passivation. Furthermore, in this paper, we have revealed the key physical parameters, such as surface recombination and charge transfer mechanisms and rates, in understanding the use of chalcopyrite/chalcogenide mixed sensitization of metal oxide nanostructured thin films not only for solar water splitting but also many other photoelectric related applications.

ACKNOWLEDGMENTS

This paper was funded by The Scientific and Technological Research Council of Turkey under the research Grants No. 315M348 and No. 119M030. Additionally, the authors would like to thank The Turkish Atomic Energy Authority and SESAME for x-ray absorption measurements. The authors would also like to express their gratitude to Assoc. Prof. S. Sebnem Cetin and Prof. Dr. Suleyman Ozcelik in the Photonics Application and Research Center—Gazi University for ellipsometry and PL measurements.

The authors declare no conflict of interest.

[1] G. A. Olah, G. K. S. Prakash, and A. Goeppert, Anthropogenic chemical carbon cycle for a sustainable future, J. Am. Chem. Soc. **133**, 12881 (2011).

[2] W. Yang, R. R. Prabhakar, J. Tan, S. D. Tilley, and J. Moon, Strategies for enhancing the photocurrent, photovoltage, and stability of photoelectrodes for photoelectrochemical water splitting, Chem. Soc. Rev. **48**, 4979 (2019).

[3] J. H. Kim, D. Hansora, P. Sharma, J. W. Jang, and J. S. Lee, Toward practical solar hydrogen production-an artificial photosynthetic leaf-to-farm challenge, Chem. Soc. Rev. **48**, 1908 (2019).

[4] L. J. Guo, J. W. Luo, T. He, S. H. Wei, and S. S. Li, Photocorrosion-Limited Maximum Efficiency of Solar Photoelectrochemical Water Splitting, Phys. Rev. Applied **10**, 064059 (2018).

[5] J. Kangsabanik and A. Alam, High-performance ternary alkali nitrides for renewable energy applications, Phys. Rev. Materials **3**, 105405 (2019).

[6] M. Pandey and K. W. Jacobsen, Promising quaternary chalcogenides as high-band-gap semiconductors for tandem photoelectrochemical water splitting devices: a computational screening approach, Phys. Rev. Materials **2**, 105402 (2018).

[7] G. Fan, X. Wang, H. Fu, J. Feng, Z. Li, and Z. Zou, Compensation of band-edge positions in titanium-doped Ta_3N_5 photoanode for enhanced water splitting performance: a first-principles insight, Phys. Rev. Materials **1**, 035403 (2017).

[8] W. J. Yin, H. Tang, S. H. Wei, M. M. Al-Jassim, J. Turner, and Y. Yan, Band structure engineering of semiconductors for enhanced photoelectrochemical water splitting: the case of TiO_2, Phys. Rev. B **82**, 045106 (2010).

[9] N. Abdullayeva, C. T. Altaf, M. Mintas, A. Ozer, M. Sankir, H. Kurt, and N. D. Sankir, Investigation of strain effects on photoelectrochemical performance of flexible ZnO electrodes, Sci. Rep. **9**, 11006 (2019).

[10] C. T. Altaf, M. Faraji, A. Kumtepe, N. Abdullayeva, N. Yilmaz, E. Karagoz, H. Kurt, M. Sankir, and N. D. Sankir, Highly efficient 3D-ZnO nanosheet photoelectrodes for

solar-driven water splitting: chalcogenide nanoparticle sensitization and mathematical modeling, J. Alloys Compd. **828**, 154472 (2020).

[11] Z. Xu, Q. R. Zheng, and G. Su, Charged states and band-gap narrowing in codoped ZnO nanowires for enhanced photoelectrochemical responses: density functional first-principles calculations, Phys. Rev. B **85**, 075402 (2012).

[12] D. Yolaçan and N. Demirci Sankir, Enhanced photoelectrochemical and photocatalytic properties of 3D-hierarchical ZnO nanostructures, J. Alloys Compd. **726**, 474 (2017).

[13] X. Sun, Q. Li, J. Jiang, and Y. Mao, Morphology-tunable synthesis of ZnO nanoforest and its photoelectrochemical performance, Nanoscale **6**, 8769 (2014).

[14] H. Peng, P. F. Ndione, D. S. Ginley, A. Zakutayev, and S. Lany, Design of Semiconducting Tetrahedral $Mn_{1-x}Zn_xO$ Alloys and Their Application to Solar Water Splitting, Phys. Rev. X **5**, 021016 (2015).

[15] V. Bermudez and A. Perez-Rodriguez, Understanding the cell-to-module efficiency gap in Cu(In, Ga)(S, Se)$_2$ photovoltaics scale-ip, Nat. Energy **3**, 466 (2018).

[16] N. D. Sankir, E. Aydin, H. Unver, E. Uluer, and M. Parlak, Preparation and characterization of cost effective spray pyrolyzed absorber layer for thin film solar cells, Sol. Energy **95**, 21 (2013).

[17] Y. C. Kim, H. J. Jeong, S. T. Kim, Y. H. Song, B. Y. Kim, J. P. Kim, B. K. Kang, J. H. Yun, and J. H. Jang, Luminescent down-shifting $CsPbBr_3$ perovskite nanocrystals for flexible Cu(In, Ga)Se_2 solar cells, Nanoscale **12**, 558 (2020).

[18] W. Shi, M. Theelen, A. Illiberi, N. Barreau, S. J. Van Der Sar, M. Butterling, H. Schut, W. Egger, M. Dickmann, C. Hugenschmidt, M. Zeman, E. Brück, and S. W. H. Eijt, Evolution and role of vacancy clusters at grain boundaries of ZnO:Al during accelerated degradation of Cu(In, Ga)Se_2 solar cells revealed by positron annihilation, Phys. Rev. Materials **2**, 105403 (2018).

[19] H. Li, J. Chen, Y. Zhang, W. Wang, and H. Gu, Efficiency enhancement of CIGS solar cells via recombination passivation, ACS Appl. Energy Mater. **3**, 9459 (2020).

[20] J. H. Kim, M. K. Kim, A. Gadisa, S. J. Stuard, M. M. Nahid, S. Kwon, S. Bae, B. Kim, G. S. Park, D. H. Won, D. K. Lee, D. W. Kim, T. J. Shin, Y. R. Do, J. Kim, W. J. Choi, H. Ade, and B. K. Min, Morphological-electrical property relation in Cu(In, Ga)(S, Se)$_2$ solar cells: significance of crystal grain growth and band grading by potassium treatment, Small **16**, 2003865 (2020).

[21] H. V. Alberto, R. C. Vilão, R. B. L. Vieira, J. M. Gil, A. Weidinger, M. G. Sousa, J. P. Teixeira, A. F. Da Cunha, J. P. Leitão, P. M. P. Salomé, P. A. Fernandes, T. Törndahl, T. Prokscha, A. Suter, and Z. Salman, Slow-muon study of quaternary solar-cell materials: single layers and *p-n* junctions, Phys. Rev. Materials **2**, 025402 (2018).

[22] A. Chirilă, P. Reinhard, F. Pianezzi, P. Bloesch, A. R. Uhl, C. Fella, L. Kranz, D. Keller, C. Gretener, H. Hagendorfer, D. Jaeger, R. Erni, S. Nishiwaki, S. Buecheler, and A. N. Tiwari, Potassium-induced surface modification of Cu(In, Ga)Se_2 thin films for high-efficiency solar cells, Nat. Mater. **12**, 1107 (2013).

[23] T. Zhang, Y. Yang, D. Liu, S. C. Tse, W. Cao, Z. Feng, S. Chen, and L. Qian, High efficiency solution-processed thin-film Cu(In, Ga)(Se, S)$_2$ solar cells, Energy Environ. Sci. **9**, 3674 (2016).

[24] C. T. Altaf, D. Yolacan, and N. D. Sankir, Decoration of 3D ZnO nanoelectrodes with $CuInS_2$ for solar water splitting, Mater. Lett. **236**, 710 (2019).

[25] J. Zhao, T. Minegishi, G. Ma, M. Zhong, T. Hisatomi, M. Katayama, T. Yamada, and K. Domen, Efficient photoelectrochemical hydrogen production over $CuInS_2$ photocathodes modified with amorphous Ni-MoS_x operating in a neutral electrolyte, Sustain. Energy Fuels **4**, 1607 (2020).

[26] Y. Li, J. Liu, X. Li, X. Wan, R. Pan, H. Rong, J. Liu, W. Chen, and J. Zhang, Evolution of hollow $CuInS_2$ nanododecahedrons via Kirkendall effect driven by cation exchange for efficient solar water splitting, ACS Appl. Mater. Interfaces **11**, 27170 (2019).

[27] B. Koo, S. W. Nam, R. Haight, S. Kim, S. Oh, M. Cho, J. Oh, J. Y. Lee, B. T. Ahn, and B. Shin, Tailoring photoelectrochemical performance and stability of Cu(In, Ga)Se_2 photocathode via TiO_2-coupled buffer layers, ACS Appl. Mater. Interfaces **9**, 5279 (2017).

[28] Ç. Tuc Altaf and N. Demirci Sankir, Colloidal synthesis of $CuInS_2$ nanoparticles: crystal phase design and thin film fabrication for photoelectrochemical solar cells, Int. J. Hydrogen Energy **44**, 18712 (2019).

[29] B. Kim, G. S. Park, S. Y. Chae, M. K. Kim, H. S. Oh, Y. J. Hwang, W. Kim, and B. K. Min, A highly efficient Cu(In, Ga)(S, Se)$_2$ photocathode without a hetero-materials overlayer for solar-hydrogen production, Sci. Rep. **8**, 5182 (2018).

[30] C. Tuc Altaf, N. S. Sahsuvar, N. Abdullayeva, O. Coskun, A. Kumtepe, E. Karagoz, M. Sankir, and N. Demirci Sankir, Inverted configuration of Cu(In, Ga)S_2/In_2S_3 on 3D-ZnO/$ZnSnO_3$ bilayer system for highly efficient photoelectrochemical water splitting, ACS Sustain. Chem. Eng. **8**, 15209 (2020).

[31] H. Kobayashi, N. Sato, M. Orita, Y. Kuang, H. Kaneko, T. Minegishi, T. Yamada, and K. Domen, Development of highly efficient $CuIn_{0.5}Ga_{0.5}Se_2$-based photocathode and application to overall solar driven water splitting, Energy Environ. Sci. **11**, 3003 (2018).

[32] C. Tuc Altaf, M. Sankir, and N. Demirci Sankir, Synthesis of Cu(In, Ga)S_2 nanoparticles via hot-injection method and incorporation with 3D-ZnO/In_2S_3 heterojunction photoanode for enhanced optical and photoelectrochemical properties, Mater. Lett. **304**, 130602 (2021).

[33] M. G. Mali, H. Yoon, B. N. Joshi, H. Park, S. S. Al-Deyab, D. C. Lim, S. J. Ahn, C. Nervi, and S. S. Yoon, Enhanced photoelectrochemical solar water splitting using a platinum-decorated CIGS/CdS/ZnO photocathode, ACS Appl. Mater. Interfaces **7**, 21619 (2015).

[34] M. Chen, Y. Liu, C. Li, A. Li, X. Chang, W. Liu, Y. Sun, T. Wang, and J. Gong, Spatial control of cocatalysts and elimination of interfacial defects towards efficient and robust CIGS photocathodes for solar water splitting, Energy Environ. Sci. **11**, 2025 (2018).

[35] W. Septina Gunawan, S. Ikeda, T. Harada, T. Minegishi, K. Domen, and M. Matsumura, Platinum and indium sulfide-modified $CuInS_2$ as efficient photocathodes for photoelectrochemical water splitting, Chem. Commun. **50**, 8941 (2014).

[36] S. Y. Kim, M. S. Mina, K. Kim, J. Gwak, and J. H. Kim, Application of a Sn^{4+} doped In_2S_3 thin film in a CIGS solar cell as a buffer layer, Sustain. Energy Fuels **4**, 362 (2019).

[37] See Supplemental Material at http://link.aps.org/supplemental/10.1103/PhysRevMaterials.5.125403 for schematic representation of the experimental procedure and surface ESEM images of ZnO nanostructured thin films, EDAX analyses of pristine and CIGS/In2S3 deposited ZnO thin films, detailed PL fitting data obtained from OriginPro 8.0 software, PEC water splitting efficiency calculations and individual performance results, EIS measurements, IMPS, electric field distribution modeling via COMSOL Multiphysics, refractive index results of CIGS and In2S3 layers.

[38] A. Kumtepe, C. T. Altaf, N. S. Sahsuvar, N. Abdullayeva, E. Koseoglu, M. Sankir, and N. D. Sankir, Indium sulfide based photoelectrodes for all-vanadium photoelectrochemical redox flow batteries, ACS Appl. Energy Mater. **3**, 3127 (2020).

[39] T. G. Mayerhöfer, S. Pahlow, and J. Popp, The Bouguer-Beer-Lambert law: shining light on the obscure, ChemPhysChem **21**, 2029 (2020).

[40] C. D. Wagner, L. H. Gale, and R. H. Raymond, Two-dimensional chemical state plots: a standardized data set for use in identifying chemical states by x-ray photoelectron spectroscopy, Anal. Chem. **51**, 466 (1979).

[41] M. Wang, F. Ren, J. Zhou, G. Cai, L. Cai, Y. Hu, D. Wang, Y. Liu, L. Guo, and S. Shen, N doping to ZnO nanorods for photoelectrochemical water splitting under visible light: engineered impurity distribution and terraced band structure, Sci. Rep. **5**, 12925 (2015).

[42] S. H. Jung, E. Oh, K. H. Lee, Y. Yang, C. G. Park, W. Park, and S. H. Jeong, Sonochemical preparation of shape-selective ZnO nanostructures, Cryst. Growth Des. **8**, 265 (2008).

[43] H. Wang, B. Wang, J. Yu, Y. Hu, C. Xia, J. Zhang, and R. Liu, Significant enhancement of power conversion efficiency for dye sensitized solar cell using 1D/3D network nanostructures as photoanodes, Sci. Rep. **5**, 9305 (2015).

[44] F. Yang, W. H. Liu, X. W. Wang, J. Zheng, R. Y. Shi, H. Zhao, and H. Q. Yang, Controllable low temperature vapor-solid growth and hexagonal disk enhanced field emission property of ZnO nanorod arrays and hexagonal nanodisk networks, ACS Appl. Mater. Interfaces **4**, 3852 (2012).

[45] R. Zhang, P. G. Yin, N. Wang, and L. Guo, Photoluminescence and Raman scattering of ZnO nanorods, Solid State Sci. **11**, 865 (2009).

[46] K. Kim, K. L. Kim, and K. S. Shin, Raman spectral characteristics of 4-aminobenzenethiol adsorbed on ZnO nanorod arrays, Phys. Chem. Chem. Phys. **15**, 9288 (2013).

[47] H. Liu, Y. Wang, J. Wu, G. Zhang, and Y. Yan, Oxygen vacancy assisted multiferroic property of Cu doped ZnO films, Phys. Chem. Chem. Phys. **17**, 9098 (2015).

[48] T. Liu, H. Xu, W. S. Chin, Z. Yong, and A. T. S. Wee, Local structural evolution of Co-doped ZnO nanoparticles upon calcination studied by *in situ* quick-scan XAFS, J. Phys. Chem. C **112**, 3489 (2008).

[49] O. M. Ozkendir, S. Yildirimcan, A. Yuzer, and K. Ocakoglu, Crystal and electronic structure study of Mn doped wurtzite ZnO nanoparticles, Prog. Nat. Sci. Mater. Int. **26**, 347 (2016).

[50] D. Chen, Z. Wang, T. Ren, H. Ding, W. Yao, R. Zong, and Y. Zhu, Influence of defects on the photocatalytic activity of ZnO, J. Phys. Chem. C **118**, 15300 (2014).

[51] Y. H. Lu, S. P. Russo, and Y. P. Feng, Effect of nitrogen and intrinsic defect complexes on conversion efficiency of ZnO for hydrogen generation from water, Phys. Chem. Chem. Phys. **13**, 15973 (2011).

[52] N. Abdullayeva, C. Tuc Altaf, A. Kumtepe, N. Yilmaz, O. Coskun, M. Sankir, H. Kurt, C. Celebi, A. Yanilmaz, and N. Demirci Sankir, Zinc oxide and metal halide perovskite nanostructures having tunable morphologies grown by nanosecond laser ablation for light-emitting devices, ACS Appl. Nano Mater. **3**, 5881 (2020).

[53] M. Chen, X. Wang, Y. H. Yu, Z. L. Pei, X. D. Bai, C. Sun, R. F. Huang, and L. S. Wen, X-ray photoelectron spectroscopy and Auger electron spectroscopy studies of Al-doped ZnO films, Appl. Surf. Sci. **158**, 134 (2000).

[54] R. Al-Gaashani, S. Radiman, A. R. Daud, N. Tabet, and Y. Al-Douri, XPS and optical studies of different morphologies of ZnO nanostructures prepared by microwave methods, Ceram. Int. **39**, 2283 (2013).

[55] J. H. Zheng, Q. Jiang, and J. S. Lian, Synthesis and optical properties of flower-like ZnO nanorods by thermal evaporation method, Appl. Surf. Sci. **257**, 5083 (2011).

[56] M. K. Singha and A. Patra, Highly efficient and reusable ZnO microflower photocatalyst on stainless steel mesh under UV-Vis and natural sunlight, Opt. Mater. (Amst). **107**, 110000 (2020).

[57] S. Ghosh and D. Basak, A simple process step for tuning the optical emission and ultraviolet photosensing properties of sol-gel ZnO film, RSC Adv. **7**, 694 (2017).

[58] K. Bandopadhyay and J. Mitra, Zn interstitials and O vacancies responsible for *n*-type ZnO: what do the emission spectra reveal? RSC Adv. **5**, 23540 (2015).

[59] D. M. Fernandes, A. A. W. Hechenleitner, S. M. Lima, L. H. C. Andrade, A. R. L. Caires, and E. A. G. Pineda, Preparation, characterization, and photoluminescence study of PVA/ZnO nanocomposite films, Mater. Chem. Phys. **128**, 371 (2011).

[60] G. E. Marques, M. D. Teodoro, and J. A. H. Coaquira, Growth and formation mechanism of shape-selective preparation of ZnO structures: correlation of structural, vibrational and optical properties, Phys. Chem. Chem. Phys. **22**, 7329 (2020).

[61] H. Zeng, G. Duan, Y. Li, S. Yang, X. Xu, and W. Cai, Blue luminescence of ZnO nanoparticles based on non-equilibrium processes: defect origins and emission controls, Adv. Funct. Mater. **20**, 561 (2010).

[62] K. Vanheusden, C. H. Seager, W. L. Warren, D. R. Tallant, and J. A. Voigt, Correlation between photoluminescence and oxygen vacancies in ZnO phosphors, Appl. Phys. Lett. **68**, 403 (1996).

[63] H. L. Guo, Q. Zhu, X. L. Wu, Y. F. Jiang, X. Xie, and A. W. Xu, Oxygen deficient ZnO_{1-x} nanosheets with high visible light photocatalytic activity, Nanoscale **7**, 7216 (2015).

[64] J. Chen, W. Liu, and W. Gao, Tuning photocatalytic activity of In_2S_3 broadband spectrum photocatalyst based on morphology, Appl. Surf. Sci. **368**, 288 (2016).

[65] R. Jayakrishnan, Photoluminescence in spray pyrolysis deposited β-In_2S_3 thin films, J. Electron. Mater. **47**, 2249 (2018).

[66] R. Jayakrishnan, T. Sebastian, C. Sudha Kartha, and K. P. Vijayakumar, Effect of defect bands in β-In_2S_3 thin films, J. Appl. Phys. **111**, 093714 (2012).

[67] X. Yu, X. An, A. Shavel, M. Ibáñez, and A. Cabot, The effect of the Ga content on the photocatalytic hydrogen evolution of $Cu\,In_{1-x}Ga_xS_2$ nanocrystals, J. Mater. Chem. A **2**, 12317 (2014).

[68] I. A. Pronin, B. V. Donkova, D. T. Dimitrov, I. A. Averin, J. A. Pencheva, and V. A. Moshnikov, Relationship between the photocatalytic and photoluminescence properties of zinc oxide doped with copper and manganese, Semiconductors **48**, 842 (2014).

[69] C. Yu, F. Chen, D. Zeng, Y. Xie, W. Zhou, Z. Liu, L. Wei, K. Yang, and D. Li, A facile phase transformation strategy for fabrication of novel Z-scheme ternary heterojunctions with efficient photocatalytic properties, Nanoscale **11**, 7720 (2019).

[70] W. Yang, Y. Oh, J. Kim, H. Kim, H. Shin, and J. Moon, Photoelectrochemical properties of vertically aligned $CuInS_2$ nanorod arrays prepared via template-assisted growth and transfer, ACS Appl. Mater. Interfaces **8**, 425 (2016).

[71] A. Hankin, F. E. Bedoya-Lora, J. C. Alexander, A. Regoutz, and G. H. Kelsall, Flat band potential determination: avoiding the pitfalls, J. Mater. Chem. A **7**, 26162 (2019).

[72] X. Lü, X. Mou, J. Wu, D. Zhang, L. Zhang, F. Huang, F. Xu, and S. Huang, Improved-performance dye-sensitized solar cells using Nb-doped TiO_2 electrodes: efficient electron injection and transfer, Adv. Funct. Mater. **20**, 509 (2010).

[73] E. Przezdziecka, E. Guziewicz, D. Jarosz, D. Snigurenko, A. Sulich, P. Sybilski, R. Jakiela, and W. Paszkowicz, Influence of oxygen-rich and zinc-rich conditions on donor and acceptor states and conductivity mechanism of ZnO films grown by ALD-experimental studies, J. Appl. Phys. **127**, 075104 (2020).

[74] I. Rodríguez-guti, A. Vega-poot, M. Rodríguez-p, R. García-rodríguez, G. Rodríguez-gattorno, and G. Oskam, Charge transfer and recombination kinetics at WO_3 for photoelectrochemical water oxidation, Electrochim. Acta **258**, 900 (2017).

[75] Y. Y. Avital, H. Dotan, D. Klotz, D. A. Grave, A. Tsyganok, B. Gupta, I. Visoly-fisher, A. Rothschild, and A. Yochelis, Two-site H_2O_2 photo-oxidation on haematite photoanodes, Nat. Commun. **9**, 4060 (2018).

[76] Y. C. Chen, H. H. Chang, and Y. K. Hsu, Synthesis of $CuInS_2$ quantum dots/In_2S_3/ZnO nanowire arrays with high photoelectrochemical activity, ACS Sustain. Chem. Eng. **6**, 10861 (2018).

[77] H. Qian, Z. Liu, Z. Guo, M. Ruan, and W. Yan, A promising ternary sulfide bidirectional *p-n* heterojunction for unassisted tandem photoelectrochemical cells, Chem. Commun. **57**, 4910 (2021).

[78] H. Wang, Y. Xia, H. Li, X. Wang, Y. Yu, X. Jiao, and D. Chen, Highly active deficient ternary sulfide photoanode for photoelectrochemical water splitting, Nat. Commun. **11**, 3078 (2020).

[79] J. S. Kim, S. K. Baek, Y. B. Kim, H. W. Do, Y. H. Kwon, S. W. Cho, Y. D. Yun, J. H. Yoon, H. B. R. Lee, S. W. Kim, and H. K. Cho, Copper indium selenide water splitting photoanodes with artificially designed heterophasic blended structure and their high photoelectrochemical performances, Nano Energy **46**, 1 (2018).

[80] Z. Cheng, X. Zhan, F. Wang, Q. Wang, and K. Xu, Nanowire arrays for efficient hydrogen generation, RSC Adv. **5**, 81723 (2015).

[81] Y. Choi, M. Beak, and K. Yong, Solar-driven hydrogen evolution using a $CuInS_2$/CdS/ZnO heterostructure nanowire array as an efficient photoanode, Nanoscale **6**, 8914 (2014).

[82] X. Shi, I. Y. Choi, K. Zhang, J. Kwon, D. Y. Kim, J. K. Lee, S. H. Oh, J. K. Kim, and J. H. Park, Efficient photoelectrochemical hydrogen production from bismuth vanadate-decorated tungsten trioxide helix nanostructures, Nat. Commun. **5**, 4775 (2014).